ACS OMEGA

http://pubs.acs.org/journal/acsodf

Article

# Partial Destabilization of Amyloid-$\beta$ Protofibril by Methionine Photo-Oxidation: A Molecular Dynamic Simulation Study

Fahimeh Maghsoodi, Tye D. Martin, and Eva Y. Chi*

Cite This: *ACS Omega* 2023, 8, 10148−10159

Read Online

ACCESS | Metrics & More | Article Recommendations | Supporting Information

**ABSTRACT:** Selective photosensitized oxidation of amyloid protein aggregates is being investigated as a possible therapeutic strategy for treating Alzheimer's disease (AD). Photo-oxidation has been shown to degrade amyloid-$\beta$ (A$\beta$) aggregates and ameliorate aggregate toxicity in vitro and reduce aggregate levels in the brains of AD animal models. To shed light on the mechanism by which photo-oxidation induces fibril destabilization, we carried out an all-atom molecular dynamics (MD) simulation to examine the effect of methionine (Met35) oxidation on the conformation and stability of a $\beta$-sheet-rich A$\beta_{9-40}$ protofibril. Analyses of up to 1 $\mu$s simulations showed that the oxidation of the Met35 residues, which resulted in the addition of hydrophilic oxygens in the fibril core, reduced the overall conformational stability of the protofibril. Specifically, Met35 disrupted the hydrophobic interface that stabilizes the stacking of the two hexamers that comprise the protofibril. The oxidized protofibril is more solvent exposed and exhibits more backbone flexibility. However, the protofibril retained the underlying U-shaped architecture of each peptide upon oxidation, and although some loss of $\beta$-sheets occurred, a significant portion remained. Our simulation results are thus consistent with our experimental observation that photo-oxidation of A$\beta$40 fibril resulted in the dis-agglomeration and fragmentation of A$\beta$ fibrils but did not cause complete disruption of the fibrillar morphology or $\beta$-sheet structures. The partial destabilization of A$\beta$ aggregates supports the further development of photosensitized platforms for the targeting and clearing of A$\beta$ aggregates as a therapeutic strategy for treating AD.

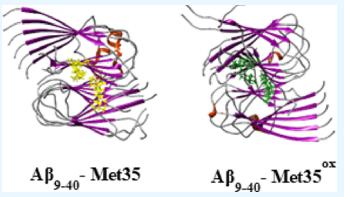


## INTRODUCTION

The abnormal aggregation and deposition of the amyloid-beta (A$\beta$) peptides into extracellular amyloid plaques is a major pathological event in the development of Alzheimer's disease (AD).[1−3] It is linked to the progressive neurodegeneration in AD[4−8] that involves the impairment of synaptic transmission and the loss of long-term potentiation.[9,10] Amyloid plaques are formed by the misfolding and aggregation of A$\beta$ into small oligomers that subsequently grow into large fibrils rich in cross $\beta$-sheets.[11,12] A$\beta$ oligomers have been found to be cytotoxic,[13−16] and A$\beta$ fibrils also contribute to neurodegeneration by impairing axonal transport[10,13] and seeding the aggregation of the tau protein to form intracellular neurofibrillary tangles.[14] Additionally, A$\beta$ aggregates are also involved in the spatiotemporal disease progression through cell-to-cell transmission.[15−17] Because of the central roles A$\beta$ aggregates play in AD pathogenesis, modulating the peptide's aggregation and inducing the selective degradation and clearance of A$\beta$ aggregates is an attractive therapeutic strategy.

Among the many approaches that have been studied, photodynamic therapy (PDT) has drawn the attention of researchers[18−20] because it is spatiotemporally controllable and minimally invasive.[21,22] PDT has been used to treat diseases since the 1960s[23] and is currently being used to treat many types of skin, lung, and esophageal cancers or pre-cancers.[24] PDT requires a photosensitizer to produce singlet oxygens, which lead to the generation of reactive oxygen species (ROS) that subsequently oxidize cellular components, including cell membranes and organelles, and induce apoptosis, which destroys diseased tissues.[25−27] In recent years, a number of studies have investigated the potential of PDT for treating AD by specifically targeting the A$\beta$ peptide.[28,29] A range of photosensitizers have been tested, and these studies have shown that photo-oxidation of monomeric (or soluble) A$\beta$ can inhibit the peptide's aggregation and that photo-oxidation of fibrillar A$\beta$ can cause fibril fragmentation and disintegration in vitro.[18,30−38] Encouragingly, A$\beta$ aggregate degradation induced by photo-oxidation has also been found to attenuate aggregate toxicity[39] and reduce aggregate levels in the brains of AD mouse models.[40] In transgenic AD models of *Caenorhabditis elegans*, photo-oxidation of A$\beta$ fibrils has been found to reduce A$\beta$ neurotoxicity and extend the longevity of *C. elegans*.[30,41]

Most of the compounds that have been studied are known photosensitizers and are non-selective, including polyoxometalate[31], 1,2,4-oxadiazole[35], tetra(4-sulfonatophenyl) porphyrin[34], rose bengal[36], methylene blue[38], and porphyrinic metal−organic frameworks[30], and induce the photo-oxidation of both A$\beta$ monomers and aggregates, as well as other biomolecules in

Received: November 21, 2022
Accepted: February 20, 2023
Published: March 10, 2023

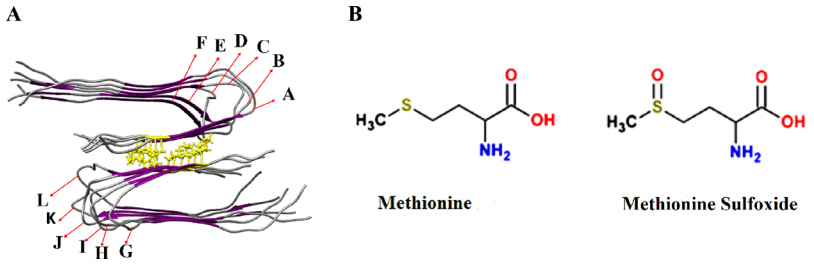


**Figure 1.** (A) Structure of dodecameric Aβ protofibril (2LMN), which consists of two hexamers. Individual $A\beta_{9-40}$ chains are denoted as A to L, and Met35 residue side chains are shown in yellow. Purple and gray in the protofibril represent β-sheets and coils, respectively. (B) Chemical structures of Met and $Met^{ox}$.

the vicinity of the photosensitizers. This causes off-target oxidation and is a major drawback of PDT.[42,43] Recently, several aggregate-selective photosensitizers have been developed and tested, including those based on fibril-binding dyes thioflavin T and curcumin[39,40,44] and highly amyloid aggregate-selective *p*-phenylene ethynylene-based florescence sensors.[45−47] These new aggregate-selective photosensitizers can potentially overcome off-target oxidation and minimize side effects in future clinical applications.

To further develop photoactive platforms that target the degradation and clearance of Aβ amyloids, a fundamental understanding of the effect of photo-oxidation on Aβ aggregates is needed. Many studies have documented the morphological changes to Aβ fibrils upon photo-oxidation, including fibril fragmentation, rupture, and disintegration.[38,39,45] Photo-oxidation sites have also been identified. However, molecular-level details of the conformational changes that lead to fibril destabilization have not been fully elucidated.

For Aβ monomers, several studies have shed light on the mechanism by which photo-oxidation attenuates the monomer's aggregation of Aβ monomers. Thioflavin T sensitized the oxidation of Tyr10, His13, His14, and Met35 residues,[48] which reduced the aggregation propensity of the monomers and delayed aggregation. An NMR study demonstrated that oxidation of Met35 in Aβ monomers considerably impeded aggregation and the propensity of β-strand formation as the addition of a hydrophilic oxygen disrupted the hydrophobic interactions that stabilize the β-strands.[49] These findings are consistent with others that found that oxidation of Met35 inhibited coil-to-β-sheet transition,[50] significantly reduced trimer and tetramer formation,[51] and slowed the rate of fibrillation.[52] In an in vivo experiment, oxidation of Met35 in $A\beta_{1-42}$ prevented the formation of a paranucleus[53] and thereby inhibited further fibrillation. Computational studies corroborated experimental findings and indicated that the oxidation of Met35 in Aβ impeded aggregation by reducing the β-strand content on the C-terminal hydrophobic region.[54]

For $A\beta_{1-40}$ fibrils, we and others have shown that photosensitization results in the oxidation of His13, His14, and Met35.[18,45,48] The histidine residues are located on the surface of Aβ fibrils, whereas Met35 residues are located in the hydrophobic core region of the fibrils. Concomitant with photo-oxidation, we observed that clumps of long fibrils disaggregated and fragmented into shorter fibrils. The shorter oxidized fibrils are non-toxic and largely retained the β-sheet structures that were present in the native fibrils and the ability to seed fibrillation of Aβ monomers.[45] Photo-oxidation of Aβ fibrils thus destabilized some structural aspects of Aβ fibrils but did not completely disassemble the aggregates. The partial stabilization can be advantageous for future therapeutic development as more complete disruption of fibrils can generate smaller oligomers that are more neurotoxic. Here, we carried out an all-atom molecular dynamics (MD) study to gain an understanding of the effect of photo-oxidation on fibril structure and stability. Although MD simulation has not been used to analyze the structures of photo-oxidized Aβ aggregates, the effects of oxidation caused by other pathways, such as through the reactive oxygen and nitrogen species produced by cold atmospheric plasma that lead to different patterns (Met35, Phe19, Phe20, Lys 16, and Lys28) and degrees of oxidation (3−15%),[55] have been investigated computationally.[56] Razzokov and co-workers found that 3% of Met35 oxidation of an $A\beta_{11-42}$ pentamer led to a small destabilization in the structure of the pentamer and further increases of oxidation levels (9 and 15%) led to higher structural fluctuations and destabilization.[56] MD simulation has also been used to study early steps of Aβ oligomer destabilization by the binding of a number of ligands.[57−60]

In this study, we carried out longer simulations (up to 1 μs) on a larger 12-chain Aβ protofibril where all Met35 residues were replaced with $Met35^{ox}$. The larger protofibril with complete Met35 oxidation better mimics photo-oxidation studies that have been carried out on fibrils, and the longer simulation time allows us to capture dynamics at longer time scales. A number of analyses were carried out to assess the effects of Met35 oxidation on protofibril conformation and dynamics. Specifically, we monitored the deviation of the protofibril from its initial structure and analyzed changes to secondary structures that stabilize the protofibril.[61−64] Global changes to the protofibril conformation were also monitored through analyzing the number of hydrogen bonds and solvent-accessible surface areas. Overall, we sought to characterize the dynamic destabilization of an Aβ protofibril due to Met35 oxidation to better understand the underlying mechanism of photo-oxidation-induced partial fibril destabilization.

## METHODS

**System Setup.** The initial structure of the Aβ protofilament ($A\beta_{9-40}$) was obtained from the Protein Data Bank (PDB ID: 2LMN), which consisted of two stacked hexamers.[65] Peptide chains are designated from A to F for the top hexamer and G to L for the bottom hexamer (Figure 1A). The Met35 residues in yellow are located in the middle of the protofibril where the hydrophobic surfaces of the two hexamers meet. The structures of Met and $Met^{ox}$ are shown in Figure 1B. Protofibrils containing either Met35 ($A\beta_{9-40}$-Met35) or oxidized Met35 ($A\beta_{9-40}$-$Met35^{ox}$) were set up.



https://doi.org/10.1021/acsomega.2c07468
ACS Omega 2023, 8, 10148−10159

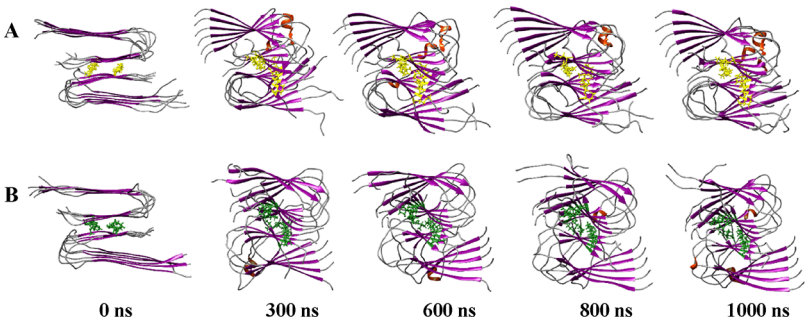


**Figure 2.** Snapshots of native (A) and oxidized (B) Aβ protofibrils from 1 μs simulations. Met35 and Met35$^{ox}$ are shown in yellow and green, respectively. β-Strands, α-helices, and coils are shown in purple, orange, and gray, respectively.

**Simulation Methods.** The initial structure and parameterization of Met35$^{ox}$ were obtained using the SWISS-PARAM web server.[66] After parameterization, MD simulations were prepared and run using Gromacs v2018[67] in isothermal (NVT) and isobaric ensembles (NPT). For water, the TIP3P model was used. Per SWISS-PARAM web server's instructions to users when we started this simulation project in 2018, the CHARMM27 force field was used. We note that CHARMM27 has been found to have an α-helical bias[68] and CHARMM36m is an improved model for modeling intrinsically disordered proteins and conformational changes.[68,69] The limitation of the CHARMM27 is somewhat mitigated since the protofibril structures simulated in this study are ordered and contains very little α-helix during the simulation (see Table S1 in the Supporting Information). To prepare Aβ$_{9-40}$-Met35$^{ox}$, each of the 12 Met35 residues in the native Aβ protofibril was substituted with a Met35$^{ox}$. A cubic simulation box of 10.8 nm in each dimension with periodic boundary conditions was used for the native and oxidized Aβ protofibrils. Sodium ions were then added to maintain charge balance.

Energy minimization of the systems was carried out using the steepest descent minimization method to reach a maximum force <1000.0 kJ/mol/nm. The energy-minimized systems were then equilibrated for 1 ns in NVT and NPT ensembles using LINCS[70] constraints for hydrogen bonds (H-bonds) with a standard leap-frog integrator selected with a 2 fs time step. van der Waals interactions were treated with a cutoff distance of 1.0 nm, and long-range electrostatic interactions were calculated using particle mesh Ewald (PME) with a 1.0 nm cutoff length.[71] For NVT equilibration, the modified Berendsen thermostat coupling was used to keep the temperature constant at 310 K. For NPT equilibration, the temperature (310 K) and pressure (1 bar) coupling was applied via the modified Berendsen thermostat coupling[72] and Parrinello−Rahman method,[73] respectively. MD productions of equilibrated systems were performed at NPT. For each system, three trajectories of 300 ns were run. The last trajectory of each system continued to run to 1 μs. UCSF chimera[74] was used for visualization, and further analyses were done using Gromacs v2018. All simulations were run on the Comet hybrid computing cluster at the Extreme Science and Engineering Discovery Environment (XSEDE) digital service at the San Diego Supercomputer Center (SDSC).[75]

**Analysis of Simulation Results.** A number of different tools provided by the Gromacs v2018 package[67] were utilized to analyze the simulation results to assess the structural stability of the protofibrils. The evaluated parameters include root mean square deviation (RMSD), root mean square fluctuation (RMSF), the radius of gyration ($R_g$), solvent-accessible surface area (SASA), the number of H-bonds (total, inter-chain, and intra-chain), and Asp23 (D23)−Lys28 (K28) salt bridge distances (inter-chain and intra-chain). Moreover, the secondary structures of the protofibrils were investigated via the Dictionary of Secondary Structure of Protein (DSSP)[76] program to assess any conformational changes to the protofibril with Met35$^{ox}$ substitutions.

RMSD was obtained based on the $C_\alpha$ atoms of the peptides for the two hexamers. The $R_g$ values of native and oxidized Aβ protofibrils were computed using the *gmx gyrate* tool. To supplement RMSD analysis, principal component analysis (PCA) was carried out via *gmx covar* and *gmx anaeig* for the last 50 ns (2500 frames) of the simulations. The GROMACS utility *gmx hbond* tool was used to compute the number of H-bonds between all main chains of the protofibril where a 0.35 nm donor−acceptor cutoff distance was assigned. To calculate the inter-chain hydrogen bonds, an index for each chain was made and the number of H-bonds between adjacent chains (for example, AB, BC, CD) was counted and added. For intra-chain H-bonds, the number of H-bonds associated with each chain was counted and added. SASA values of the protofibrils were calculated for all simulations. The distance between Met35 residues of opposing chains (A and G, B and H, C and I, D and J, E and K, F and L) in native and oxidized protofibrils was determined and compared. *gmx mak_ndx* was used to create appropriate index files separating Met35 residues of opposing Aβ chain pairs for all simulation trajectories. For contact map analysis, *gmx mdmat* was used to generate minimal distance matrices between pairs of residues.

## RESULTS

The fibrillar conformation of the Aβ peptide is highly thermodynamically stable and is primarily stabilized by the extended β-sheet core. To gain insights into the early structural changes to Aβ fibrils caused by photo-oxidation, which ultimately lead to fibril destabilization, we focused our analysis on the oxidation of Met35 as it is located in the fibril core and is expected to have the most significant impact on fibril structure and stability. A large Aβ$_{9-40}$ protofibril with two stacked hexamers was chosen in this study as it contains the salient structural features of Aβ amyloid polymorphs, the U-shaped architecture of each Aβ peptide, extended inter-sheet chain-to-chain contacts, and hydrophobic strand-to-strand contacts.[77] We first examined snapshots of native and oxidized protofibril trajectories. Then, we calculated RMSD, $R_g$, SASA, and RMSF values to evaluate structural fluctuations and possible expansion of the protofibril. Secondary structures, the


https://doi.org/10.1021/acsomega.2c07468
ACS Omega 2023, 8, 10148−10159

number of H-bonds, and salt bridge interactions were also analyzed to gain more insights into the effects of Met35 oxidation.

**Dynamics of Native and Oxidized Aβ Protofibrils.** Snapshots of native ($A\beta_{40}$-Met35) and oxidized ($A\beta_{40}$-Met35$^{ox}$) Aβ protofibrils from the 1 μs simulations are shown in Figure 2. Snapshots from the 300 ns trajectories are shown in Figure S1 of the Supporting Information. As shown, both protofibrils undergo structural changes with simulation time and become less ordered compared to the energy-minimized structures at the beginning of the simulations (0 ns). The extended β-sheets started to twist along the protofibril axis such that some of the β-strands are no longer co-planar by the end of the simulations. Chains located at the edges of the protofibrils appeared to have moved the most.

To better visualize chain movements of the $A\beta_{40}$-Met35 and $A\beta_{40}$-Met35$^{ox}$ protofibrils, the end chains (A and L) in both protofibrils were highlighted and compared at the end of the 1 μs simulations (Figure 3). As shown, chain A (magenta) in the native protofibril is twisted but largely retained its β-hairpin structure (Figure 3A) whereas the same chain in the oxidized protofibril is also twisted but the β-hairpin is less aligned (Figure 3C). At the other end of the protofibril, chain L (blue) in the native protofibril is twisted along the protofibril axis and lost some of its β-sheet characteristics (Figure 3B). In comparison, chain L in the oxidized protofibril is more twisted along the protofibril axis (Figure 3D). Although this chain largely retained its hairpin structure, intra-chain β-sheet contacts are lost as well as the inter-chain β-sheet contacts with the adjacent chain K in the protofibril. Note that a few α-helices were observed to form in the turn region of both the native and oxidized protofibril (Figures 2 and 3, Figure S1, and Table S1). Because of the α-helical bias of the CHARMM27 force field,[68] these α-helices can be potential artifacts.

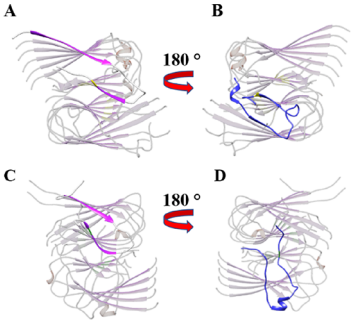


**Figure 3.** Visualization of end chains A (magenta) and L (blue) of the native (A and B) and the oxidized (C and D) Aβ protofibrils at 1000 ns of simulation time. Structures in A and C are each rotated at 180° to visualize the other ends of the protofibrils. The rest of the chains are colored gray for better visualization of the end chains.

Overall, snapshots of the protofibrils showed that both protofibrils largely retained their aggregated structure. Although the difference between $A\beta_{40}$-Met35 and $A\beta_{40}$-Met35$^{ox}$ protofibrils in these snapshots is not large, the twisting of chains was observed more frequently and at a higher degree in the $A\beta_{40}$-Met35$^{ox}$ protofibril compared to the $A\beta_{40}$-Met35 protofibril.

**Structural Stability of Native and Oxidized Aβ Protofibrils.** To assess the global conformational stabilities of the two protofibrils, we performed several analyses, including calculating the Cα-RMSD, $R_g$, SASA, and RMSF values of the 300 ns and 1 μs trajectories. RMSD values of the short (300 ns) and long (1 μs) simulations are shown in Figure 4A and B, respectively. Averaged RMSD values from the last 50 ns of each simulation are summarized in Table 1. Our results show that the oxidized protofibril generally exhibited higher RMSD values compared to the native protofibril, particularly at longer simulation times. This trend is also generally supported by PCA, where the oxidized protofibril occupies increased phase space (Figure S2 and S3), indicating increased flexibility.

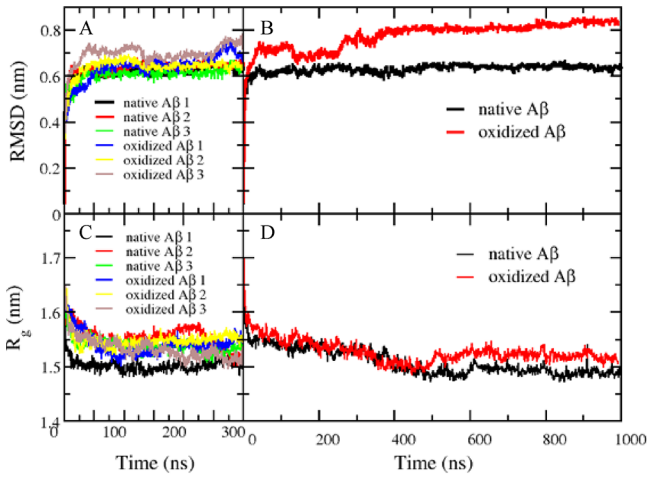


**Figure 4.** RMSD (A, B) and $R_g$ (C, D) plots of native and oxidized protofibrils from 300 ns (A, C) and 1 μs (B, D) simulations. RMSD and $R_g$ values shown for the 300 ns simulations (A and C) are averages from three simulation trajectories.

The $R_g$ of the native and oxidized protofibrils over the 300 ns and 1 μs trajectories are shown in Figure 4C and D, respectively, and summarized in Table 1. $R_g$ values are calculated from the mass-weighted spatial distribution of the atoms in the protofibril and can be interpreted as a measure of the structural compactness of the protofibril. Both native and oxidized protofibrils exhibited similar $R_g$ values of around 1.52 during the 300 ns trajectories. After 400 ns of simulation however, $R_g$ values for the oxidized protofibril were slightly higher than those of the native protofibril (Figure 4D), implying that Met35 oxidation slightly decreased the compactness of the protofibril.

SASA is another important property that gives information about the overall protein conformation in an aqueous environment. Proteins are composed of hydrophobic and hydrophilic residues and tend to adopt structures that minimize the exposure of hydrophobic residues to the aqueous solvent. Increases in SASA from a stable state can indicate protein instability, such as unfolding that exposes hydrophobic residues to the solvent, which can lead to further undesirable changes such as irreversible aggregation.[78] Substitution of amino acids, whether mutational or chemical, can also disturb the native conformation of a protein and result in partial unfolding, which leads to increases in SASA.

In this study, SASA values for the protofibrils were computed. As shown in Figure 5A,B and Table 1, SASA values of the oxidized protofibril were larger than those of the native protofibril; the average SASA values computed from the last 50 ns of the 1 μs simulations for the native and oxidized Aβ protofibrils were 180.46 ± 3.24 and 197.57 ± 2.96 $nm^2$,


https://doi.org/10.1021/acsomega.2c07468
ACS Omega 2023, 8, 10148−10159

**Table 1. Averaged Values, with Associated Standard Deviations of Backbone RMSD, $R_g$, SASA, and Number of H-Bonds for the Native and Oxidized A$\beta$ Protofibrils from the Last 50 ns (2500 Frames) of Trajectories**

| protofibril and simulation trajectory | | RMSD (nm) | $R_g$ (nm) | SASA of protofibril (nm$^2$) | number of inter-chain H-bonds | number of intra-chain H-bonds | total number of H-bonds |
|---|---|---|---|---|---|---|---|
| native A$\beta_{9-40}$ | trajectory 1 (300 ns) | 0.63 ± 0.011 | 1.51 ± 0.007 | 184.73 ± 3.67 | 177.2 ± 4.4 | 46.9 ± 4.2 | 242.8 ± 7.0 |
| | trajectory 2 (300 ns) | 0.64 ± 0.010 | 1.53 ± 0.012 | 189.91 ± 3.95 | 174.9 ± 4.4 | 43.8 ± 4.5 | 234.0 ± 6.1 |
| | trajectory 3 (300 ns) | 0.63 ± 0.017 | 1.53 ± 0.006 | 181.06 ± 3.78 | 182.2 ± 4.4 | 51.0 ± 4.2 | 245.9 ± 6.6 |
| | trajectory 4 (1 $\mu$s) | 0.63 ± 0.009 | 1.49 ± 0.005 | 180.46 ± 3.24 | 178.4 ± 5.4 | 49.3 ± 3.9 | 243.8 ± 6.9 |
| oxidized A$\beta_{9-40}$-Met35$^{ox}$ | trajectory 1 (300 ns) | 0.71 ± 0.021 | 1.55 ± 0.009 | 197.29 ± 2.93 | 166.9 ± 5.3 | 38.3 ± 3.3 | 224.5 ± 6.1 |
| | trajectory 2 (300 ns) | 0.65 ± 0.012 | 1.56 ± 0.006 | 193.72 ± 3.28 | 161.8 ± 4.1 | 37.1 ± 3.8 | 223.7 ± 6.4 |
| | trajectory 3 (300 ns) | 0.74 ± 0.019 | 1.52 ± 0.008 | 199.20 ± 3.95 | 162.0 ± 4.7 | 40.3 ± 5.0 | 214.0 ± 7.3 |
| | trajectory 4 (1 $\mu$s) | 0.84 ± 0.0070 | 1.51 ± 0.007 | 197.57 ± 2.96 | 160.4 ± 4.3 | 48.1 ± 4.0 | 223.6 ± 6.6 |

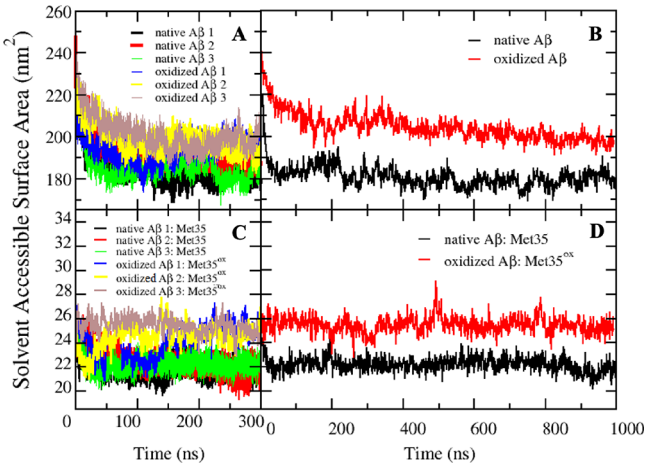


**Figure 5.** Solvent-accessible surface area (SASA) values of the native (black) and oxidized (red) protofibrils calculated from 300 ns (A) and 1 $\mu$s (B) simulation trajectories. SASA values of the Met35 (black) or Met35$^{ox}$ (red) residue in native and oxidized A$\beta$ protofibrils calculated from 300 ns (C) and 1 $\mu$s (D) simulations.

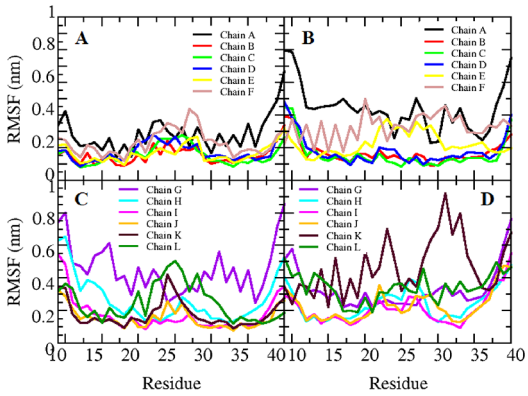


**Figure 6.** RMSF plots of different A$\beta$ chains belonging to the top hexamer (chains A to F: A and B) and bottom hexamer (chains G to L: C and D) of the native (A and C) and oxidized (B and D) protofibrils after 1 $\mu$s of simulation.

respectively. Met35 oxidation thus caused about 17 nm$^2$ or 10% increase of protofibril SASA. To assess the effect of oxidation on solvent exposure of the Met35 residue, SASA values of the Met35 or Met35$^{ox}$ residues for all simulation trajectories were also calculated (Figure 5C,D). As shown, Met35$^{ox}$, located in the core of the protofibril, showed higher (by about 4 nm$^2$) SASA values compared to Met35 in the native protofibril. Oxidation of Met to methionine sulfoxide increases the hydrophilicity of the residue, and even though Met is deeply buried in the hydrophobic core of the protofibril, its solvent exposure increased. However, the ~4 nm$^2$ increase in Met35 SASA only partially contributes to the overall ~17 nm$^2$ increase in protofibril SASA, indicating that oxidation of the Met35 at the core of the protofibril might have caused global conformational changes to the protofibril such that the oxidized structure is in a more solvent exposed state.

To evaluate the local dynamics and flexibility of each residue of the A$\beta$ chains, the RMSF values of the backbone of A$\beta$ in the top hexamer (chains A to F) and bottom hexamer (chains G to L) for native and oxidized protofibrils after 1 $\mu$s of simulation were calculated and are plotted in Figure 6. RMSF plots of the 300 ns simulations are shown in Figure S4 of the Supporting Information. As expected, terminal chains A and F of the top hexamer and chains G and L of the bottom hexamer showed higher fluctuations with higher RMSF values than the interior chains (Figure 6A,C). Moreover, in the oxidized protofibril, 8 out of 12 chains (chains A, E, F, G, I, J, K, and L) showed statistically significant higher RMSF values compared to the native protofibril ($p < 0.05$). Some of these chains are terminal chains, and some are in the interior of the protofibril. As such, our results show that Met35 oxidation caused increased chain flexibilities throughout the protofibril.

Taken together, our analyses of the global conformational characteristics of a native A$\beta_{40}$-Met35 and an oxidized A$\beta_{40}$-Met35$^{ox}$ protofibrils indicate that Met35 oxidation has a destabilizing effect on the highly ordered protofibril structure, wherein the A$\beta_{40}$-Met35$^{ox}$ protofibril showed higher values of RMSD, SASA, and RMSF compared to those of the A$\beta_{40}$-Met35 protofibril. $R_g$ values were minimally affected. Both protofibrils deviated from the initial energy-minimized structures wherein twisting and misalignment of the $\beta$-strands were observed during simulations.

**Methionine−Methionine Distances in the Protofibril Core.** The hydrophobic interactions of Met35 residues from the two opposing hexamers facilitate the favorable interaction of the two hexamers in the native protofibril (Figure 1). This


https://doi.org/10.1021/acsomega.2c07468
ACS Omega 2023, 8, 10148−10159

parallel transversal combination of the two hexamers around the longitudinal axis of the protofibril is a common feature of various polymorphisms identified in the A$\beta$ fibril architecture[79] and serves to shield hydrophobic residues at the C-termini of the A$\beta$ peptides. Theoretical and experimental works have shown that residues Ile31, Met35, and Val39 are involved in the hydrophobic interface of both A$\beta$40 and A$\beta$42 fibrils.[77,80−83]

Because of the important role Met35 plays in stabilizing the fibril structure, we analyzed the packing of the Met35 residues in the protofibril core by measuring the distances between Met35 and Met35 residues in the native protofibril and between Met35$^{ox}$ and Met35$^{ox}$ residues in the oxidized protofibrils; results from the 1 $\mu$s simulations are summarized in Figure 7. The same plots for the 300 ns simulations are shown in Figure S5 of the Supporting Information. As shown in Figure 7, except for the end chains A and G, all other Met35−Met35 pairs equilibrated to 0.8 to 1 nm distances in the native protofibril. The end chains A and G showed greater Met35−Met35 distances of around 1.8 nm during most of the simulation and dropped to around 1 nm after 800 ns of simulation. This greater fluctuation is consistent with higher RMSF values observed for the two chains (Figure 6A,C). Met35$^{ox}$−Met35$^{ox}$ distances in oxidized fibrils in general showed more fluctuations during the simulations. In particular, interior chain pairs, C and I, D and J, and E and K, showed statistically significant higher Met35$^{ox}$−Met35$^{ox}$ distances than Met35−Met35 distances in the native protofibril ($p < 0.05$), while the end chain pairs (A and G, F, and L) and the near end-chain pair (B and H) did not show significant differences in Met-Met distances.

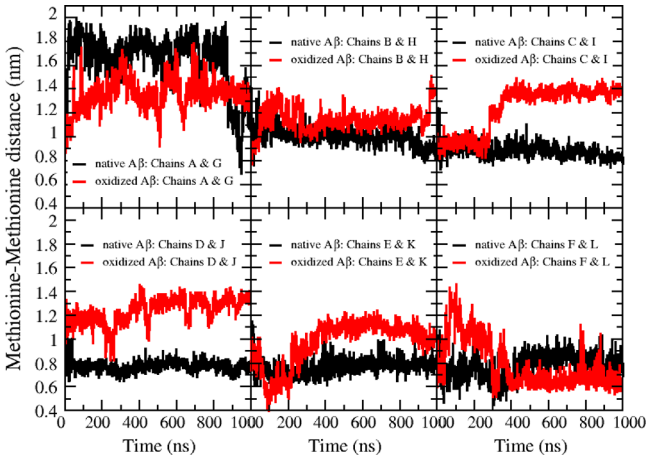


**Figure 7.** Distances between Met35 and Met35 (black) and between Met35$^{ox}$ and Met35$^{ox}$ (red) residues of six opposing A$\beta$ chain pairs (A and G, B and H, C and I, D and J, E and K, and F and L) in the protofibrils for the 1 $\mu$s simulation.

The trends in methionine−methionine distances suggest that the oxidation of the most buried methionine residues of the central chains away from protofibril ends had the biggest impact in disrupting the fibril structure. This finding also suggests that the increase in SASA of the protofibril with oxidation (Figure 5) can be due to increased solvent exposure of the interior Met35 residues upon oxidation.

**Intra- and Inter-Peptide Salt Bridge Distances in Protofibrils.** The Asp23−Lys29 (D23−K28) salt bridge that forms near the turn region of the A$\beta$ peptide plays an important role in stabilizing the U-shaped $\beta$-strand-turn-$\beta$-strand motif of the peptide and prevents large backbone motion. We performed an analysis of the D23−K28 salt bridge distances in the native and oxidized protofibrils to assess if Met35 oxidation adversely affected the stability of the intra-peptide salt bridges. D23−K28 distances for each A$\beta$ chain for the 1 $\mu$s simulations are shown in Figure S6. Comparisons between salt bridge distances of the native protofibril and oxidized fibrils did not show a consistent trend. Distances are comparable for chains E, G, H, I, and L. They are larger in the oxidized protofibril than the native protofibril for chains J and K but smaller for chains A, C, and D. Thus overall, Met35 oxidation did not have a consistent effect on intra-molecular salt bridge distances, and these salt bridges appear to be relatively unaffected by Met35 oxidation.

We also analyzed the inter-peptide D23−K28 salt bridges formed by adjacent A$\beta$ peptides for the 1 $\mu$s simulation (Figure S7). These salt bridges also stabilize the peptides' U-shape conformation and contributes to the rigidity of the A$\beta$ protofibril. As shown in Figure S7, no consistent trend emerged. Some inter-chain salt bridge distances were decreased by Met35 oxidation (chains C and D, G and H, and D and K), some remained unchanged (chains B and C, D and K, I and J) and, in one neighboring pair, increased (chains J and K). Overall, our analysis of intra- and inter-salt bridge distances thus showed that oxidation did not have a significantly destabilizing effect on the turn region of the A$\beta$ peptides' U-shape motif, nor did it destabilize the stacking of peptides in the protofibril axial direction in each of the hexamers.

**Hydrogen Bonds in Protofibrils.** Experimental and theoretical investigations have shown that the extended $\beta$-sheet conformation of the A$\beta$ protofibril and fibril is stabilized by a network of H-bonds, both intra- and inter-peptides.[82,84] The U-shape motif of each A$\beta$ peptide in the protofibril is stabilized by H-bonds that form between the two $\beta$-strands. The peptides then stack axially via hydrogen bonds to form the extended inter-peptide $\beta$-sheet structure of the fibrils and protofibrils, with the hydrophilic surface composed of N-terminal amino acids facing the solvent and the hydrophobic surface composed of C-terminal amino acids facing the interior of the fibril and protofibril core.[85−87] To study the effect of Met35 oxidation on the H-bond network of the protofibril, we calculated the total number of H-bonds (Figure 8 and Table 1) as well as the inter- and intra-chain H-bonds (Figures S8 and

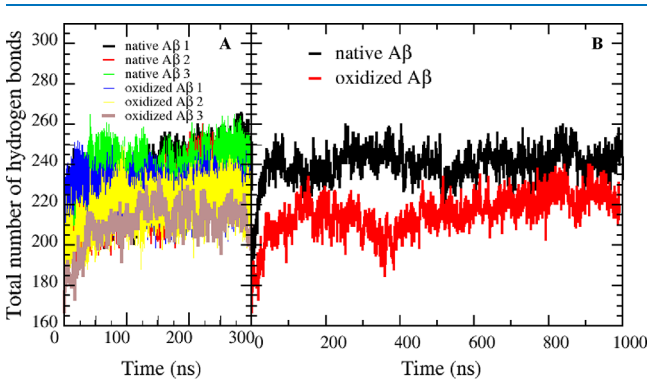


**Figure 8.** The total number of hydrogen bonds in the native protofibril (black) and the Met35-oxidized protofibrils (red) for the 300 ns (A) and 1 $\mu$s (B) simulations.



https://doi.org/10.1021/acsomega.2c07468
ACS Omega 2023, 8, 10148−10159

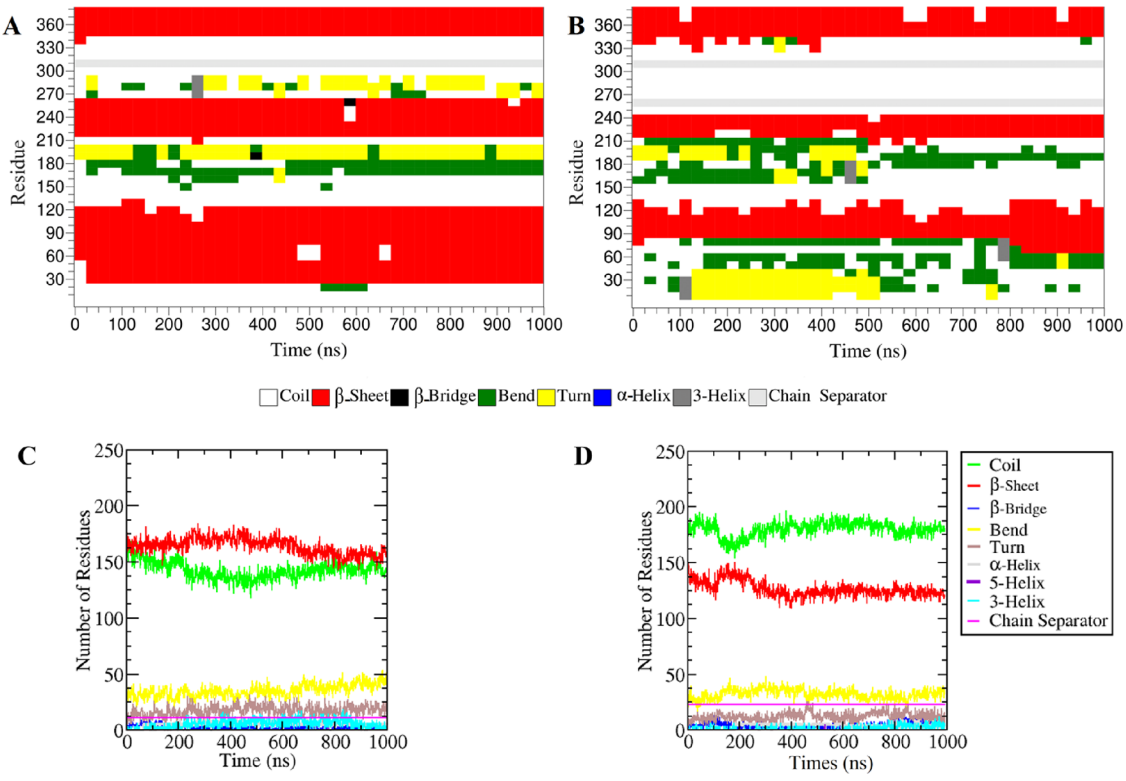


**Figure 9.** Secondary structure analysis of native and oxidized A$\beta$ protofibrils for the 1 $\mu$s simulations. DSSP mapping of native (A) and oxidized (B) A$\beta$ protofibrils show the secondary structures adopted by each amino acid of the 12 A$\beta$ peptides that form the protofibril. Secondary structure plots of native (C) and oxidized (D) A$\beta$ protofibrils show the number of amino acids that adopt each of the secondary structural elements.

S9) of the native and oxidized protofibrils as a reduction in the number of H-bonds that destabilize $\beta$-sheets, which can lead to the destabilization of the A$\beta$ protofibril structure.

As shown in Figure 8 and Table 1, the oxidized protofibril has a lower total number of H-bonds compared to the native protofibril. The difference is clear in the longer 1 $\mu$s simulations where the native protofibril has an average of 244 H-bonds compared to an average of 223 H-bonds in the oxidized protofibril over the last 50 ns of the simulations (Table 1). Oxidation of the Met35 residues in the core of the protofibril thus caused about a 10% reduction in the H-bond network in the whole protofibril.

To gain more insights into the type of H-bonds that were lost due to Met35 oxidation, we analyzed the number of intra- and inter-H-bonds (Figures S8 and S9 and Table 1). As shown, the number of inter-chain H-bonds of the oxidized protofibril is lower compared to that of the native protofibril while the numbers of intra-chain H-bonds between the oxidized and native protofibrils were comparable. Thus, H-bonds lost due to Met35 oxidation were primarily inter-chain H-bonds. In addition, we have also performed contact map analysis. As shown in Figure S11, the oxidized fibrils (Figure S11B, D) showed modest increases in pairwise distances compared to the native, unoxidized protofibril, which point to a less well-packed structure.

**Secondary Structures of A$\beta$ Protofibrils.** The A$\beta$ protofibril adopts a highly ordered conformation wherein the peptides primarily form $\beta$-sheets. A secondary structural analysis thus gives us insights into the effect of Met35 oxidation on the structural stability of the protofibril. We employed the DSSP method[76] to map the secondary structures of both native and oxidized protofibrils for the simulations (Figure 9A,B). Secondary structure plots were also constructed from the analysis (Figure 9C,D and Figure S10), and results are summarized in Table S1.

As shown in Figure 9A, the predominate secondary structures in the native protofibril were $\beta$-sheets (red) and coils (white), followed by turns (yellow) and bends (green). In the oxidized protofibril, the level of $\beta$-sheets was reduced, accompanied by a notable increase in the level of coils (Figure 9B). These changes are more easily visualized in plots of secondary structures of the native (Figure 9C) and oxidized (Figure 9D) protofibrils and by the averaged percentages of the secondary structures from the last 50 ns of trajectories (Table S1). As the other secondary structures remained largely at the same low levels in the oxidized fibrils, the photo-oxidation of Met35 appeared to mainly have a disruptive effect on some $\beta$-sheets in the protofibril and did not cause the significant formation of other, ordered secondary structures such as $\alpha$-helices.

## DISCUSSION

Photosensitizer-induced oxidation of A$\beta$ aggregates is being explored as a promising therapeutic strategy for the targeted degradation and clearance of the aggregates. Photo-oxidized fibrils exhibit lower toxicity in vitro, and importantly, photo-oxidation has been reported to reduce brain A$\beta$ aggregate levels and extend the longevity of AD animal models.[30,40,41] We have shown in a recent in vitro study that a fibril-selective photosensitizer caused clumps of A$\beta$40 fibrils to dissociate and fragment into smaller fibrils with light irradiation.[45] Moreover, the oxidized fibrils retained a significant amount of $\beta$-sheet structures of the native fibrils and the ability to seed the aggregation of A$\beta$ monomers. This partial fibril destabilization


https://doi.org/10.1021/acsomega.2c07468
ACS Omega 2023, 8, 10148−10159

may be advantageous since more complete degradation of amyloid fibrils can potentially result in oligomers that are more toxic compared to fibrillar Aβ conformers.[88,89] In order to better understand photo-sensitized fibril degradation and clearance and further develop PDT to treat AD, a detailed understanding of the effect of photo-oxidation on fibril structure and stability is needed.

In this study, we performed all-atom MD simulations to investigate the effect of Met35 oxidation on the structural dynamics and stability of an $A\beta_{9-40}$ protofibril. Simulation snapshots show that the oxidized protofibril retained its aggregated structure (Figure 1). Twisting of Aβ chains along the protofibril axis and some loss of β-sheet contacts were observed in both native and oxidized protofibrils. However, chain twisting was observed more frequently and at a higher degree in the oxidized protofibril compared to the native protofibril. β-Sheet loss is also more apparent in the oxidized protofibril. Analyses of the global conformational states of the native and oxidized protofibrils indicate that Met35 oxidation has a destabilizing effect on the highly ordered and compact protofibril structure. Compared to the native protofibril, the oxidized protofibril showed increased backbone Cα-RMSD and SASA. In addition, 8 out of 12 chains of the oxidized protofibril showed higher residue RMSF values compared to the native protofibril, indicating that many residues in the oxidized protofibril exhibit higher flexibility.

Further analysis of the specific interactions that stabilize the extended-β-sheet protofibril conformation shows that although the oxidized protofibril contains fewer inter-chain H-bonds and β-sheets, the intra-chain salt bridges and intra-chain H-bonds that stabilize the U shape of each peptide and the inter-chain salt bridges stabilize the stacking of the peptides in each of the hexamers were largely unperturbed. Met35 photo-oxidation thus did not exhibit a significant destabilizing effect in the U shape of the peptides or the stacking of the peptides in the hexamers. It did, however, disrupt the hydrophobic interactions between the two hexamers as the $Met35^{ox}$–$Met35^{ox}$ distances are larger for the interior, most hydrophobic, chains compared to Met35–Met35 distances. This finding is also consistent with increases in SASA values of the oxidized protofibril.

The MD simulation results from this study thus indicate that the oxidation of Met35 caused partial destabilization to the overall conformation of the protofibril. Specifically, Met35 oxidation that resulted in the addition of a hydrophilic oxygen disrupted the hydrophobic interface that stabilizes the stacking of the two hexamers. The oxidized protofibril is more solvent exposed and has more backbone flexibility but retained the underlying U-shaped structure of each peptide. Although more twisting of the peptides along the protofibril axis was observed, the stacking of the peptides in the hexamers remained with Met35 oxidation. Our simulation results are consistent with experimental observations that photo-oxidation of Aβ40 fibril results in the dis-agglomeration and fragmentation of Aβ fibrils but did not cause complete disruption of the fibrillar morphology or β-sheets.[45] We note, however, that photo-sensitized oxidation also leads to the oxygenation of two histidine residues (His13 and His14) and their effects are not included in this computational study. The addition of hydrophilic oxygens to the imidazole ring of histidine can also disrupt their hydrophobic interactions and contribute to fibril destabilization. Also, the 2LMN dodecamer structure lacks eight N-terminal residues. In a first resolved fibril structure that contains the N-terminal residues, Söldner and coworkers found in an MD study that these residues had a clear stabilizing effect where Arg5, Asp7, and Ser8 formed interfilament contacts that stabilized a threefold symmetric fibril structure derived from patients.[90] Future studies that include oxidized His residues and full-length peptides will further resolve the effects of photo-oxidation on fibril stability. To capture possible large-range structural changes, longer simulation times, perhaps coupled with course-graining or enhanced sampling methods, can also be performed in the future.

The partial destabilization of preformed Aβ fibrils observed in our photo-oxidation study differs from that where Aβ fibrils were oxidized by chemical oxidants (e.g., oxidation of $A\beta_{1-42}$ fibrils by $H_2O_2$ that caused remodeling of the fibrillar morphology to irregularly shaped rope-like structures and globules[91]) or where Aβ fibrils are destabilized by the binding of ligands (e.g., caffeine, brazilin, a resveratrol derivative, and wine-related polyphenols that completely disaggregated pre-formed Aβ fibrils into disordered monomers in vitro[92−94]). Consistent with experimental results, MD simulation of the binding of caffeine to an $A\beta_{17-42}$ pentamer showed destabilization of the pentamer conformation and loss of H-bonds and β-sheet structures as well as salt bridges.[57] A recent MD simulation study examined the effects of oxidation of five different residues (Met35, Phe19, Ph20, Lys16, Lys28) on the stability of an $A\beta_{11-42}$ pentamer via umbrella sampling.[56] This particular oxidation pattern was experimentally achieved by a pulsed radio-frequency cold atmospheric plasma jet that caused the complete disintegration of $A\beta_{1-42}$ fibrils.[56] The high level of oxidation was found in the simulation study to disrupt salt bridges and cause significant disturbance to the pentamer structure.[56] This simulation study also showed that a low and moderate degree of oxidation (one (Met35) or three (Met35, Phe19, and Phe20) oxidized amino acids) had insignificant impact on the pentamer conformation and did not disrupt salt bridges, which is consistent with our findings in this study.

## CONCLUSIONS

We studied the effects of Met35 oxidation on the conformation and stability of a $A\beta_{9-40}$ protofibril, employing all-atom MD simulations for up to 1 μs. The results demonstrate that the oxidation of Met35 caused some destabilization to the overall conformation of the β-sheet-rich protofibril, as evidenced in increases in RMSD, SASA, and RMSF values. The oxidized protofibril is thus more solvent exposed and has more backbone flexibility, which may be contributed by the destabilization of the hydrophobic interface that stabilize the stacking of two hexamers in the protofibril as evidenced by increased methionine−methionine distances in the oxidized protofibril. However, Met35 oxidation did not significantly perturb the intra- and inter-chain salt bridges that stabilize the U-shaped conformation adopted by each chain or the stacking of the peptides that form each of the hexamers. These simulation results are consistent with experimental findings that photo-oxidation caused partial destabilization of Aβ40 fibrils and did not completely disrupt the conformation and underlying secondary structures of the Aβ aggregate. This is in contrast with oxidation caused by chemical oxidants or strong oxidizing sources such as cold atmospheric plasma. This computational study thus provides molecular level insights into the partial perturbations of Aβ40 aggregates by photo-


https://doi.org/10.1021/acsomega.2c07468
ACS Omega 2023, 8, 10148−10159

sensitizer-induced oxidation. Combined with in vivo studies that demonstrated the efficacy of PDT in lowering aggregate levels and reducing neurotoxicity of Aβ aggregates in AD animal models, this investigation contributes to our future development of photo-active platforms for treating protein misfolding diseases such as AD.

## ■ ASSOCIATED CONTENT

### Supporting Information

The Supporting Information is available free of charge at https://pubs.acs.org/doi/10.1021/acsomega.2c07468.

(Table S1) Secondary structures (% residues), with associated standard deviations, for the native and oxidized Aβ protofibrils obtained from the last 50 ns (2500 frames) of trajectories; (Figure S1) snapshots of native and oxidized Aβ protofibrils from three 300 ns simulation trajectories; (Figure S2) principal component analysis (PCA) results obtained for the native and oxidized Aβ protofibrils from the last 50 ns (2500 frames) of the three 300 ns simulations; (Figure S3) principal component analysis (PCA) results obtained for the native and oxidized Aβ protofibrils from the last 50 ns (2500 frames) of the 1 μs simulations; (Figure S4) RMSF plots of different Aβ chains of the protofibrils; (Figure S5) distances between Met35 and Met35 and between Met35ox and Met35ox residues of six opposing Aβ chain pairs in the protofibrils; (Figure S6) profiles of the intra-chain Asp23−Lys28 (D23−K28) salt bridge distances of Aβ chain in the native and oxidized protofibrils for the 1 μs simulations; (Figure S7) distances of inter-peptide salt bridges formed by Asp23 and Lys28 (D23-K28) on adjacent Aβ peptides for native and oxidized protofibrils for the 1 μs simulations; (Figure S8) total number of inter-chain hydrogen bonds in the native protofibril and the Met35 oxidized protofibrils. Figure S9. The number of intra-chain hydrogen bonds in the native protofibril and the Met35-oxidized protofibrils; (Figure S10) secondary structure plots of native and oxidized Aβ protofibrils for the three 300 ns simulations; (Figure S11) matrix of smallest distance between each pair of amino acids in native (A and C) and Met35 oxidized (C and D) protofibrils over the 1 μs for the last 50 ns of simulations (PDF)

## ■ AUTHOR INFORMATION


### Corresponding Author

**Eva Y. Chi** − *Center for Biomedical Engineering and Department of Chemical and Biological Engineering, University of New Mexico, Albuquerque, New Mexico 87131, United States;* orcid.org/0000-0001-7448-9943; Phone: 505-277-2263; Email: evachi@unm.edu

### Authors

**Fahimeh Maghsoodi** − *Nanoscience and Microsystems Engineering Graduate Program and Center for Biomedical Engineering, University of New Mexico, Albuquerque, New Mexico 87131, United States*

**Tye D. Martin** − *Center for Biomedical Engineering, University of New Mexico, Albuquerque, New Mexico 87131, United States;* orcid.org/0000-0002-0987-0606

Complete contact information is available at: https://pubs.acs.org/10.1021/acsomega.2c07468


### Author Contributions

F.M., T.D.M., and E.Y.C designed the research; F.M. performed research and analyzed results; F.M and E.Y.C wrote the paper.


### Funding

This research was funded by the National Science Foundation (NSF) Awards 1605225 and 1207362, and the National Institute of Health (NIH) Award 1R21NS111267-01 to E.Y.C. We would also like to acknowledge generous gifts from the Huning family and others from the State of New Mexico.


### Notes

The authors declare no competing financial interest.

## ■ ACKNOWLEDGMENTS

The Extreme Science and Engineering Discovery Environment (XSEDE), which is supported by National Science Foundation grant ACI-1053575, was used for performing simulations.

## ■ ABBREVIATIONS

Aβ: amyloid β; AD: Alzheimer's disease; MD: molecular dynamics; PDT: photodynamic therapy; ROS: reactive oxygen species; NMR: nuclear magnetic resonance; His: histidine; Tyr: tyrosine; Met: methionine; PDB: Protein Data Bank; NVT: isothermal ensemble; NPT: isobaric ensemble; LINCS: A Linear Constraint Solver for Molecular Simulations; PME: particle mesh Ewald; RMSD: root mean square deviation; RMSF: root mean square fluctuation; $R_g$: radius of gyration; SASA: solvent-accessible surface area; DSSP: Dictionary of Secondary Structure of Protein; XSEDE: Extreme Science and Engineering Discovery Environment

## ■ REFERENCES


(1) O'Brien, R. J.; Wong, P. C. Amyloid Precursor Protein Processing and Alzheimer's Disease. *Annu. Rev. Neurosci.* **2011**, *34*, 185−204.

(2) Murphy, M. P.; Levine, H. Alzheimer's Disease and the Beta-Amyloid Peptide. *J. Alzheimer's Dis.* **2010**, *19*, 311−323.

(3) Lesné, S.; Koh, M. T.; Kotilinek, L.; Kayed, R.; Glabe, C. G.; Yang, A.; Gallagher, M.; Ashe, K. H. A Specific Amyloid-Beta Protein Assembly in the Brain Impairs Memory. *Nature* **2006**, *440*, 352−357.

(4) Hardy, J.; Selkoe, D. J. The Amyloid Hypothesis of Alzheimer's Disease: Progress and Problems on the Road to Therapeutics. *Science* **2002**, *297*, 353−356.

(5) Karran, E.; Mercken, M.; De Strooper, B. The Amyloid Cascade Hypothesis for Alzheimer's Disease: An Appraisal for the Development of Therapeutics. *Nat. Rev. Drug. Discovery* **2011**, *10*, 698−712.

(6) Kayed, R.; Head, E.; Thompson, J. L.; Mcintire, T. M.; Milton, S. C.; Cotman, C. W.; Glabel, C. G. Common Structure of Soluble Amyloid Oligomers Implies Common Mechanism of Pathogenesis. *Science* **2003**, *300*, 486−489.

(7) Reitz, C. Alzheimer's Disease and the Amyloid Cascade Hypothesis: A Critical Review. *Int. J. Alzheimers Dis.* **2012**, *2012*, 1.

(8) Bloom, G. S. Amyloid-β and Tau: The Trigger and Bullet in Alzheimer Disease Pathogenesis. *JAMA Neurol.* **2014**, *71*, 505−508.

(9) Sheng, M.; Sabatini, B. L.; Südhof, T. C. Synapses and Alzheimer's Disease. *Cold Spring Harbor Perspect. Biol.* **2012**, *4*, 1−18.

(10) Parihar, M. S.; Brewer, G. J. Amyloid-β as a Modulator of Synaptic Plasticity. *J. Alzheimer's Dis.* **2010**, *22*, 741−763.

(11) Sachse, C.; Fändrich, M.; Grigorieff, N. Paired β-Sheet Structure of an Aβ(1-40) Amyloid Fibril Revealed by Electron Microscopy. *Proc. Natl. Acad. Sci.* **2008**, *105*, 7462−7466.

(12) Chen, G. F.; Xu, T. H.; Yan, Y.; Zhou, Y. R.; Jiang, Y.; Melcher, K.; Xu, H. E. Amyloid Beta: Structure, Biology and Structure-Based

Therapeutic Development. *Acta Pharmacol. Sin.* **2017**, *38*, 1205−1235.
(13) Meyer-Luehmann, M.; Spires-Jones, T. L.; Prada, C.; Garcia-Alloza, M.; De Calignon, A.; Rozkalne, A.; Koenigsknecht-Talboo, J.; Holtzman, D. M.; Bacskai, B. J.; Hyman, B. T. Rapid Appearance and Local Toxicity of Amyloid-$\beta$ Plaques in a Mouse Model of Alzheimer's Disease. *Nature* **2008**, *451*, 720−724.
(14) He, Z.; Guo, J. L.; McBride, J. D.; Narasimhan, S.; Kim, H.; Changolkar, L.; Zhang, B.; Gathagan, R. J.; Yue, C.; Dengler, C.; Stieber, A.; Nitla, M.; Coulter, D. A.; Abel, T.; Brunden, K. R.; Trojanowski, J. Q.; Lee, V. M. Y. Amyloid-$\beta$ Plaques Enhance Alzheimer's Brain Tau-Seeded Pathologies by Facilitating Neuritic Plaque Tau Aggregation. *Nat. Med.* **2018**, *24*, 29−38.
(15) Cushman, M.; Johnson, B. S.; King, O. D.; Gitler, A. D.; Shorter, J. Prion-like Disorders: Blurring the Divide between Transmissibility and Infectivity. *J. Cell Sci.* **2010**, *123*, 1191−1201.
(16) Guo, J. L.; Lee, V. M. Y. Cell-to-Cell Transmission of Pathogenic Proteins in Neurodegenerative Diseases. *Nat. Med.* **2014**, *20*, 130−138.
(17) Kfoury, N.; Holmes, B. B.; Jiang, H.; Holtzman, D. M.; Diamond, M. I. Trans-Cellular Propagation of Tau Aggregation by Fibrillar Species. *J. Biol. Chem.* **2012**, *287*, 19440−19451.
(18) Taniguchi, A.; Sasaki, D.; Shiohara, A.; Iwatsubo, T.; Tomita, T.; Sohma, Y.; Kanai, M. Attenuation of the Aggregation and Neurotoxicity of Amyloid-b Peptides by Catalytic Photooxygenation. *Angew. Chem., Int. Ed.* **2014**, *53*, 1382−1385.
(19) Li, C.; Wang, J.; Liu, L. Alzheimer's Therapeutic Strategy: Photoactive Platforms for Suppressing the Aggregation of Amyloid $\beta$ Protein. *Front. Chem.* **2020**, *8*, 509.
(20) Xu, Y.; Xiao, L. Efficient Suppression of Amyloid-$\beta$ Peptide Aggregation and Cytotoxicity with Photosensitive Polymer Nanodots. *J. Mater. Chem. B* **2020**, *8*, 5776−5782.
(21) Yang, Y.; Tu, J.; Yang, D.; Raymond, J. L.; Roy, R. A.; Zhang, D. Photo- and Sono-Dynamic Therapy: A Review of Mechanisms and Considerations for Pharmacological Agents Used in Therapy Incorporating Light and Sound. *Curr. Pharm. Des.* **2019**, *25*, 401−412.
(22) Da Silva, L. P.; Magalhães, C. M.; Núñez-Montenegro, A.; Ferreira, P. J. O.; Duarte, D.; Rodríguez-Borges, J. E.; Vale, N.; Esteves Da Silva, J. C. G. Study of the Combination of Self-Activating Photodynamic Therapy and Chemotherapy for Cancer Treatment. *Biomolecules* **2019**, *9*, 384.
(23) Kessel, D. Photodynamic Therapy: From the Beginning. *Photodiagn. Photodyn. Ther.* **2004**, *1*, 3−7.
(24) Van Straten, D.; Mashayekhi, V.; de Bruijn, H. S.; Oliveira, S.; Robinson, D. J. Oncologic Photodynamic Therapy: Basic Principles, Current Clinical Status and Future Directions. *Cancers* **2017**, *9*, 19.
(25) Redza-Dutordoir, M.; Averill-Bates, D. A. Activation of Apoptosis Signalling Pathways by Reactive Oxygen Species. *Biochim. Biophys. Acta, Mol. Cell Res.* **2016**, *1863*, 2977−2992.
(26) Plaetzer, K.; Kiesslich, T.; Oberdanner, C.; Krammer, B. Apoptosis Following Photodynamic Tumor Therapy: Induction, Mechanisms and Detection. *Curr. Pharm. Des.* **2005**, *11*, 1151−1165.
(27) Lemasters, J. J. Dying a Thousand Deaths: Redundant Pathways from Different Organelles to Apoptosis and Necrosis. *Gastroenterology* **2005**, *129*, 351−360.
(28) Sohma, Y.; Sawazaki, T.; Kanai, M. Organic & Biomolecular Chemistry Chemical Catalyst-Promoted Photooxygenation of Amyloid Proteins. *Org. Biomol. Chem.* **2021**, *19*, 10017−10029.
(29) Lee, B. I.; Chung, Y. J.; Park, C. B. Photosensitizing Materials and Platforms for Light-Triggered Modulation of Alzheimer's $\beta$-Amyloid Self-Assembly. *Biomaterials* **2019**, *190-191*, 121−132.
(30) Yu, D.; Guan, Y.; Bai, F.; Du, Z.; Gao, N.; Ren, J.; Qu, X. Metal−Organic Frameworks Harness Cu Chelating and Photo-oxidation Against Amyloid $\beta$ Aggregation in Vivo. *Chem. − Eur. J.* **2019**, *25*, 3489−3495.
(31) Li, M.; Xu, C.; Ren, J.; Wang, E.; Qu, X. Photodegradation of $\beta$-Sheet Amyloid Fibrils Associated with Alzheimer's Disease by Using Polyoxometalates as Photocatalysts. *Chem. Commun.* **2013**, *49*, 11394−11396.
(32) Yue, X.; Mei, Y.; Zhang, Y.; Tong, Z.; Cui, D.; Yang, J.; Wang, A.; Wang, R.; Fei, X.; Ai, L.; et al. New Insight into Alzheimer's Disease: Light Reverses A$\beta$-Obstructed Interstitial Fluid Flow and Ameliorates Memory Decline in APP/PS1 Mice. *Alzheimer's Dementia: Transl. Res. Clin. Interv.* **2019**, *5*, 671−684.
(33) Tardivo, J. P.; Del Giglio, A.; De Oliveira, C. S.; Gabrielli, D. S.; Junqueira, H. C.; Tada, D. B.; Severino, D.; De Fátima Turchiello, R.; Baptista, M. S. Methylene Blue in Photodynamic Therapy: From Basic Mechanisms to Clinical Applications. *Photodiagn. Photodyn. Ther.* **2005**, *24*, 175−191.
(34) Lee, B. I.; Lee, S.; Suh, Y. S.; Lee, J. S.; Kim, A. K.; Kwon, O. Y.; Yu, K.; Park, C. B. Photoexcited Porphyrins as a Strong Suppressor of $\beta$-Amyloid Aggregation and Synaptic Toxicity. *Angew. Chem., Int. Ed.* **2015**, *127*, 11634−11638.
(35) Mangione, M. R.; Palumbo Piccionello, A.; Marino, C.; Ortore, M. G.; Picone, P.; Vilasi, S.; Di Carlo, M.; Buscemi, S.; Bulone, D.; San Biagio, P. L. Photo-Inhibition of A$\beta$ Fibrillation Mediated by a Newly Designed Fluorinated Oxadiazole. *RSC Adv.* **2015**, *5*, 16540−16548.
(36) Lee, J. S.; Lee, B. I.; Park, C. B. Photo-Induced Inhibition of Alzheimer's $\beta$-Amyloid Aggregation Invitro by Rose Bengal. *Biomaterials* **2015**, *38*, 43−49.
(37) Kim, K.; Lee, S. H.; Choi, D. S.; Park, C. B. Alzheimer's Disease: Photoactive Bismuth Vanadate Structure for Light-Triggered Dissociation of Alzheimer's $\beta$-Amyloid Aggregates. *Adv. Funct. Mater.* **2018**, *28*, No. 1870298.
(38) Lee, B. I.; Suh, Y. S.; Chung, Y. J.; Yu, K.; Park, C. B. Shedding Light on Alzheimer's $\beta$-Amyloidosis: Photosensitized Methylene Blue Inhibits Self-Assembly of $\beta$-Amyloid Peptides and Disintegrates Their Aggregates. *Sci. Rep.* **2017**, *7*, 7523.
(39) Taniguchi, A.; Shimizu, Y.; Oisaki, K.; Sohma, Y.; Kanai, M. Switchable Photooxygenation Catalysts That Sense Higher-Order Amyloid Structures. *Nat. Chem.* **2016**, *8*, 974−982.
(40) Nagashima, N.; Ozawa, S.; Furuta, M.; Oi, M.; Hori, Y.; Tomita, T.; Sohma, Y.; Kanai, M. Catalytic Photooxygenation Degrades Brain A$\beta$ in Vivo. *Sci. Adv.* **2021**, *7*, No. eabc9750.
(41) Du, Z.; Gao, N.; Wang, X.; Ren, J.; Qu, X. Near-Infrared Switchable Fullerene-Based Synergy Therapy for Alzheimer's Disease. *Small* **2018**, *14*, No. 1801852.
(42) Dos Santos, A. F.; De Almeida, D. R. Q.; Terra, L. F.; Baptista, M. S.; Labriola, L. Photodynamic Therapy in Cancer Treatment - an Update Review. *J. Cancer Metastasis Treat.* **2019**, *2019*, 25.
(43) Dolmans, D. E. J. G. J.; Fukumura, D.; Jain, R. K. Photodynamic Therapy for Cancer. *Nat. Rev. Cancer* **2003**, *3*, 380−387.
(44) Ni, J.; Taniguchi, A.; Ozawa, S.; Hori, Y.; Kuninobu, Y.; Saito, T.; Saido, T. C.; Tomita, T.; Sohma, Y.; Kanai, M. Near-Infrared Photoactivatable Oxygenation Catalysts of Amyloid Peptide. *Chem* **2018**, *4*, 807−820.
(45) Fanni, A. M.; Okoye, D.; Monge, F. A.; Hammond, J.; Maghsoodi, F.; Martin, T. D.; Brinkley, G.; Phipps, M. L.; Evans, D. G.; Martinez, J. S.; Whitten, D. G.; Chi, E. Y. Controlled and Selective Photo-Oxidation of Amyloid-$\beta$ Fibrils by Oligomeric p -Phenylene Ethynylenes. *ACS Appl. Mater. Interfaces* **2022**, *14*, 14871−14886.
(46) Monge, F.; Fanni, A.; Jiang, S.; Whitten, D. G.; Bhaskar, K.; Chi, E. Y. Luminescent Molecular Sensors for the Selective Detection of Neurodegenerative Disease Protein Pathology in CSF. *Biophys. J.* **2019**, *116*, 146a−147a.
(47) Donabedian, P. L.; Pham, T. K.; Whitten, D. G.; Chi, E. Y. Oligo(p-Phenylene Ethynylene) Electrolytes: A Novel Molecular Scaffold for Optical Tracking of Amyloids. *ACS. Chem. Neurosci.* **2015**, *6*, 1526−1535.
(48) Ahn, M.; Lee, B. I.; Chia, S.; Habchi, J.; Kumita, J. R.; Vendruscolo, M.; Dobson, C. M.; Park, C. B. Chemical and Mechanistic Analysis of Photodynamic Inhibition of Alzheimer's $\beta$-Amyloid Aggregation. *Chem. Commun.* **2019**, *55*, 1152−1155.
(49) Hou, L.; Shao, H.; Zhang, Y.; Li, H.; Menon, N. K.; Neuhaus, E. B.; Brewer, J. M.; Byeon, I. J. L.; Ray, D. G.; Vitek, M. P.; Iwashita, T.; Makula, R. A.; Przybyla, A. B.; Zagorski, M. G. Solution NMR


https://doi.org/10.1021/acsomega.2c07468
*ACS Omega* 2023, 8, 10148−10159

Studies of the Aβ(1-40) and Aβ(1-42) Peptides Establish That the Met35 Oxidation State Affects the Mechanism of Amyloid Formation. *J. Am. Chem. Soc.* **2004**, *126*, 1992−2005.
(50) Watson, A. A.; Fairlie, D. P.; Craik, D. J. Solution Structure of Methionine-Oxidized Amyloid β-Peptide (1-40). Does Oxidation Affect Conformational Switching? *Biochemistry* **1998**, *37*, 12700−12706.
(51) Palmblad, M.; Westlind-Danielsson, A.; Bergquist, J. Oxidation of Methionine 35 Attenuates Formation of Amyloid β-Peptide 1-40 Oligomers. *J. Biol. Chem.* **2002**, *277*, 19506−19510.
(52) Friedemann, M.; Helk, E.; Tiiman, A.; Zovo, K.; Palumaa, P.; Tõugu, V. Effect of Methionine-35 Oxidation on the Aggregation of Amyloid-β Peptide. *Biochem. Biophys. Rep.* **2015**, *3*, 94−99.
(53) Bitan, G.; Tarus, B.; Vollers, S. S.; Lashuel, H. A.; Condron, M. M.; Straub, J. E.; Teplow, D. B. A Molecular Switch in Amyloid Assembly: Met35 and Amyloid β-Protein Oligomerization. *J. Am. Chem. Soc.* **2003**, *125*, 15359−15365.
(54) Brown, A. M.; Lemkul, J. A.; Schaum, N.; Bevan, D. R. Simulations of Monomeric Amyloid β-Peptide (1-40) with Varying Solution Conditions and Oxidation State of Met35: Implications for Aggregation. *Arch. Biochem. Biophys.* **2014**, *545*, 44−52.
(55) Bayliss, D. L.; Walsh, J. L.; Shama, G.; Iza, F.; Kong, M. G. Reduction and Degradation of Amyloid Aggregates by a Pulsed Radio-Frequency Cold Atmospheric Plasma Jet. *New J. Phys.* **2009**, *11*, No. 115024.
(56) Razzokov, J.; Yusupov, M.; Bogaerts, A. Oxidation Destabilizes Toxic Amyloid Beta Peptide Aggregation. *Sci. Rep.* **2019**, *9*, 5476.
(57) Gupta, S.; Dasmahapatra, A. K. Caffeine Destabilizes Preformed Aβ Protofilaments: Insights from All Atom Molecular Dynamics Simulations. *Phys. Chem. Chem. Phys.* **2019**, *21*, 22067−22080.
(58) Nie, R. Z.; Cai, S.; Yu, B.; Fan, W. Y.; Li, H. H.; Tang, S. W.; Huo, Y. Q. Molecular Insights into the Very Early Steps of Aβ1-42 Pentameric Protofibril Disassembly by PGG: A Molecular Dynamics Simulation Study. *J. Mol. Liq.* **2022**, *361*, No. 119638.
(59) Singh, K.; Kaur, A.; Goyal, D.; Goyal, B. Mechanistic Insights into the Mitigation of Aβ Aggregation and Protofibril Destabilization by a D-Enantiomeric Decapeptide Rk10. *Phys. Chem. Chem. Phys.* **2022**, *24*, 21975−21994.
(60) Gao, D.; Wan, J.; Zou, Y.; Gong, Y.; Dong, X.; Xu, Z.; Tang, J.; Wei, G.; Zhang, Q. The Destructive Mechanism of Aβ1−42 Protofibrils by Norepinephrine Revealed via Molecular Dynamics Simulations. *Phys. Chem. Chem. Phys.* **2022**, *24*, 19827−19836.
(61) Wang, Q.; Wang, Y.; Lu, H. P. Revealing the Secondary Structural Changes of Amyloid β Peptide by Probing the Spectral Fingerprint Characters. *J. Raman. Spectrosc.* **2013**, *44*, 670−674.
(62) Simmons, L. K.; May, P. C.; Tomaselli, K. J.; Rydel, R. E.; Fuson, K. S.; Brigham, E. F.; Wright, S.; Lieberburg, I.; Becker, G. W.; Brems, D. N. Secondary Structure of Amyloid β Peptide Correlates with Neurotoxic Activity in Vitro. *Mol. Pharmacol.* **1994**, *45*, 373−379.
(63) Bitan, G.; Vollers, S. S.; Teplow, D. B. Elucidation of Primary Structure Elements Controlling Early Amyloid β-Protein Oligomerization. *J. Biol. Chem.* **2003**, *278*, 34882−34889.
(64) Bitan, G.; Kirkitadze, M. D.; Lomakin, A.; Vollers, S. S.; Benedek, G. B.; Teplow, D. B. Amyloid β-Protein (Aβ) Assembly: Aβ40 and Aβ42 Oligomerize through Distinct Pathways. *Proc. Natl. Acad Sci.* **2003**, *100*, 330−335.
(65) Paravastu, A. K.; Leapman, R. D.; Yau, W.-M.; Tycko, R. Molecular Structural Basis for Polymorphism in Alzheimer's β-Amyloid Fibrils. *Proc. Natl. Acad. Sci.* **2008**, *105*, 18349−18354.
(66) Zoete, V.; Cuendet, M. A.; Grosdidier, A.; Michielin, O. SwissParam: A Fast Force Field Generation Tool for Small Organic Molecules. *J. Comput. Chem.* **2011**, *32*, 2359−2368.
(67) Abraham, M. J.; Murtola, T.; Schulz, R.; Páll, S.; Smith, J. C.; Hess, B.; Lindah, E. Gromacs: High Performance Molecular Simulations through Multi-Level Parallelism from Laptops to Supercomputers. *SoftwareX* **2015**, *1-2*, 19−25.
(68) Best, R. B.; Zhu, X.; Shim, J.; Lopes, P. E. M.; Mittal, J.; Feig, M.; MacKerell, A. D., Jr. Optimization of the Additive CHARMM All-Atom Protein Force Field Targeting Improved Sampling of the Backbone φ, ψ and Side-Chain X1 and X2 Dihedral Angles. *J. Chem. Theory Comput.* **2012**, *8*, 3257−3273.
(69) Huang, J.; Rauscher, S.; Nawrocki, G.; Ran, T.; Feig, M.; de Groot, B. L.; Grubmüller, H.; MacKerell, A. D., Jr. CHARMM36m: An Improved Force Field for Folded and Intrinsically Disordered Proteins. *Nat. Methods* **2017**, *14*, 71−73.
(70) Hess, B.; Bekker, H.; Berendsen, H. J. C.; Fraaije, J. G. E. M. LINCS: A Linear Constraint Solver for Molecular Simulations. *J. Comput. Chem.* **1997**, 1463, DOI: 10.1002/(SICI)1096-987X(199709)18:12<1463::AID-JCC4>3.0.CO;2-H.
(71) Darden, T.; York, D.; Pedersen, L. Particle Mesh Ewald: An N·log(N) Method for Ewald Sums in Large Systems. *J. Chem. Phys.* **1993**, *98*, 10089−10092.
(72) Berendsen, H. J. C.; Postma, J. P. M.; Van Gunsteren, W. F.; Dinola, A.; Haak, J. R. Molecular Dynamics with Coupling to an External Bath. *J. Chem. Phys.* **1984**, *81*, 3684−3690.
(73) Nosé, S.; Klein, M. L. Constant Pressure Molecular Dynamics for Molecular Systems. *Mol. Phys.* **1983**, *50*, 1055−1076.
(74) Pettersen, E. F.; Goddard, T. D.; Huang, C. C.; Couch, G. S.; Greenblatt, D. M.; Meng, E. C.; Ferrin, T. E. UCSF Chimera - A Visualization System for Exploratory Research and Analysis. *J. Comput. Chem.* **2004**, *25*, 1605−1612.
(75) Towns, J.; Cockerill, T.; Dahan, M.; Foster, I.; Gaither, K.; Grimshaw, A.; Hazlewood, V.; Lathrop, S.; Lifka, D.; Peterson, G. D.; Roskies, R.; Scott, J. R.; Wilkens-Diehr, N. XSEDE: Accelerating Scientific Discovery. *Comput. Sci. Eng.* **2014**, *16*, 62−74.
(76) Kabsch, W.; Sander, C. Dictionary of Protein Secondary Structure: Pattern Recognition of Hydrogen-bonded and Geometrical Features. *Biopolymers* **1983**, *22*, 2577−2637.
(77) Berhanu, W. M.; Hansmann, U. H. E. Structure and Dynamics of Amyloid-β Segmental Polymorphisms. *PLoS One* **2012**, *7*, No. e41479.
(78) Kendrick, B. S.; Carpenter, J. F.; Cleland, J. L.; Randolph, T. W. A Transient Expansion of the Native State Precedes Aggregation of Recombinant Human Interferon-γ. *Proc. Natl. Acad. Sci.* **1998**, *95*, 14142−14146.
(79) Stroud, J. C.; Liu, C.; Teng, P. K.; Eisenberg, D. Toxic Fibrillar Oligomers of Amyloid-β Have Cross-β Structure. *Proc. Natl. Acad. Sci.* **2012**, *109*, 7717−7722.
(80) Kahler, A.; Sticht, H.; Horn, A. H. C. Conformational Stability of Fibrillar Amyloid-Beta Oligomers via Protofilament Pair Formation - A Systematic Computational Study. *PLoS One* **2013**, *8*, No. e70521.
(81) Sato, T.; Kienlen-Campard, P.; Ahmed, M.; Liu, W.; Li, H.; Elliott, J. I.; Aimoto, S.; Constantinescu, S. N.; Octave, J.-N.; Smith, S. O. Inhibitors of Amyloid Toxicity Based on Beta-Sheet Packing of Abeta40 and Abeta42. *Biochemistry* **2006**, *45*, 5503−5516.
(82) Zheng, J.; Jang, H.; Ma, B.; Tsai, C. J.; Nussinov, R. Modeling the Alzheimer Aβ17-42 Fibril Architecture: Tight Intermolecular Sheet-Sheet Association and Intramolecular Hydrated Cavities. *Biophys. J.* **2007**, *93*, 3046−3057.
(83) Liu, F. F.; Liu, Z.; Bai, S.; Dong, X. Y.; Suna, Y. Exploring the Inter-Molecular Interactions in Amyloid-β Protofibril with Molecular Dynamics Simulations and Molecular Mechanics Poisson-Boltzmann Surface Area Free Energy Calculations. *J. Chem. Phys.* **2012**, *136*, No. 04B610.
(84) Sunde, M.; Serpell, L. C.; Bartlam, M.; Fraser, P. E.; Pepys, M. B.; Blake, C. C. F. Common Core Structure of Amyloid Fibrils by Synchrotron X-Ray Diffraction. *J. Mol. Biol.* **1997**, *273*, 729−739.
(85) Brogi, S.; Butini, S.; Maramai, S.; Colombo, R.; Verga, L.; Lanni, C.; De Lorenzi, E.; Lamponi, S.; Andreassi, M.; Bartolini, M.; et al. Disease-Modifying Anti-Alzheimer's Drugs: Inhibitors of Human Cholinesterases Interfering with β-Amyloid Aggregation. *CNS. Neurosci. Ther.* **2014**, *20*, 624−632.
(86) Boyle, A. L.; Woolfson, D. N. De Novo Designed Peptides for Biological Applications. *Chem. Soc. Rev.* **2011**, *40*, 4295−4306.
(87) Ranganathan, S.; Gribskov, M.; Nakai, K.; Schönbach, C. *Encyclopedia of Bioinformatics and Computational Biology: ABC of bioinformatic*, Academic Press: Elsevier, 2018; pp. 661−676.


https://doi.org/10.1021/acsomega.2c07468
*ACS Omega* 2023, 8, 10148−10159

(88) Thapa, A.; Jett, S. D.; Chi, E. Y. Curcumin Attenuates Amyloid-$\beta$ Aggregate Toxicity and Modulates Amyloid-$\beta$ Aggregation Pathway. *ACS Chem. Neurosci.* **2016**, *7*, 56−68.
(89) Reiss, A. B.; Arain, H. A.; Stecker, M. M.; Siegart, N. M.; Kasselman, L. J. Amyloid Toxicity in Alzheimer's Disease. *Rev. Neurosci.* **2018**, *29*, 6130−6627.
(90) Söldner, C. A.; Sticht, H.; Horn, A. H. C. Role of the N-Terminus for the Stability of an Amyloid-$\beta$ Fibril with Three-Fold Symmetry. *PLoS One* **2017**, *12*, No. e0186347.
(91) Hou, L.; Lee, H. G.; Han, F.; Tedesco, J. M.; Perry, G.; Smith, M. A.; Zagorski, M. G. Modification of Amyloid-B1-42 Fibril Structure by Methionine-35 Oxidation. *J. Alzheimer's Dis.* **2013**, *37*, 9−18.
(92) Mao, F.; Yan, J.; Li, J.; Jia, X.; Miao, H.; Sun, Y.; Huang, L.; Li, X. New Multi-Target-Directed Small Molecules against Alzheimer's Disease: A Combination of Resveratrol and Clioquinol. *Org. Biomol. Chem.* **2014**, *12*, 5936−5944.
(93) Du, W. J.; Guo, J. J.; Gao, M. T.; Hu, S. Q.; Dong, X. Y.; Han, Y. F.; Liu, F. F.; Jiang, S.; Sun, Y. Brazilin Inhibits Amyloid $\beta$-Protein Fibrillogenesis, Remodels Amyloid Fibrils and Reduces Amyloid Cytotoxicity. *Sci. Rep.* **2015**, *5*, 1−10.
(94) Ono, K.; Yoshiike, Y.; Takashima, A.; Hasegawa, K.; Naiki, H.; Yamada, M. Potent Anti-Amyloidogenic and Fibril-Destabilizing Effects of Polyphenols in Vitro: Implications for the Prevention and Therapeutics of Alzheimer's Disease. *J. Neurochem.* **2003**, *87*, 172−181.


https://doi.org/10.1021/acsomega.2c07468
*ACS Omega* 2023, 8, 10148−10159